JACOBS UNIVERSITY BREMEN

BACHELOR'S THESIS

Modeling Stenotic Channel Flow using the Lattice Boltzmann Method

Author:
Alexandru MIHAI

Supervisors:
Prof. Dr. Tobias PREUSSER
Dr. Hanieh MIRZAEE

A thesis submitted in fulfillment of the requirements for the degree of Bachelor of Science

in the

Department of Mathematics

May 2015

JACOBS UNIVERSITY BREMEN

Abstract

Modeling Stenotic Channel Flow using the Lattice Boltzmann Method

by Alexandru MIHAI

The study of computational fluid dynamics (CFD) is growing rapidly, and one of the main models being used is the Lattice Boltzmann method. The Lattice Boltzmann Method provides an accessible avenue to analyze and model complex fluid dynamics. We analyze the flow through a constricted channel in two dimensions using the LBGK collision model. There are currently no analytic solutions known for the flow through such a geometry. We investigated the transition period of Reynolds numbers where the flow is neither laminar nor turbulent as well as the boundary conditions necessary to produce a stable simulation, as detailed in Zou and He [1]. Initial results show that this transition period occurs for Reynolds numbers of approximately 1000 to 1500 and that velocity boundaries [1] produce less numerical aberrations.

Using the open source library OpenLB and building upon the work done last semester in Guided Research a time dependent model simulating one cardiac cycle through a three dimensional geometry was created. The simulated results were compared to experimental velocity profiles found using 4D Flow MRI [2] and striking similarities were found implying a physically correct model capable of modeling more complex geometries or medical scenarios. The project was implemented in C++ with the aid of the OpenLB library and the analysis completed using MEVISFlow and ParaView.

Contents

List of Figures

1 Medical Motivation

The main motivation of this work comes from the medical phenomena of aortic coarctation, a narrowing of the aortic arch. One of the causes is genetic predisposition, but it can also be the result of plaque build-up on the arterial walls or coagulatory factors. Generally, coarctation of the aorta is discovered in children and infants but various degrees of the disease occur in the adult population as well. Its treatment is generally recommended but because its symptoms range from increased blood pressure in the upper body to decreased blood pressure in the lower body, it tends to be difficult to diagnose in adulthood. These cases are currently being dealt with on a case by case basis where information is limited with respect to which treatment options should be implemented. The treatments range from the insertion of a stent, to open the artery, to surgically removing the area, to blood thinning drugs. Each of these treatments has both pros and cons; a shunt will decrease the elasticity of the vessel but is very stable, surgically removing a part of the blood vessel is dangerous but generally does not have adverse longterm effects, and lastly medication to change the viscosity of the patient's blood causes turbulence problems that we do not completely understand (it may even prove to have severe adverse effects in some cases) but it does provide a non-invasive solution.

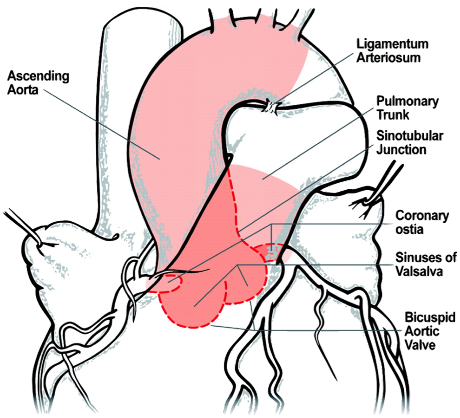

FIGURE 1: Sketch of the heart and aorta with descriptions (Source: American Heart Association)

The aorta, as seen in Figure 1, supplies blood to most of the major bodily systems. Specifically, following the ascending aorta branches form to supply blood to the brain, neck, and heart itself as seen above. Thus, an aortic stenosis after the aortic arch, following the aforementioned branches, can be a serious danger. The complex fluid dynamics that occur before and after the stenosis can lead to serious harm and therefore need to be analyzed further. Specifically, a drop in pressure or increase in velocity across the stenosis are often seen in such geometries. With a better understanding of the turbulence patterns that occur, medical professionals would be able to make a more informed decision with regards to possible treatment plans. In this thesis we are modeling this aortic stenosis using Computational Fluid Dynamics (CFD) through two simplified geometries in three dimensions as well as a simple two dimensional model.

2 Introduction

2.1 Lattice Gas Automata

The first modeling attempt of fluid dynamics using a cellular automata type model was proposed by Hardy, Pomeau, and de Pazzis in their 1973 paper [4]. It described a square lattice on which particles traveled from node to node with a fixed velocity. The *particles* are defined so that at each node a single particle can be moving in any of the four directions. The model is made up of two main steps: the collision and the transport/propagation step. In the collision step a verification is performed to check if particles are interacting with each other or the boundary walls. Namely, if two particles experience a head-on collision they are rotated by ninety degrees and propagated forward; particles interact with the walls simply by reversing their direction. All other interactions between particles yield no dynamics. If one implements such a system with an arbitrary number of initial particles it does propagate and display certain dynamic characteristic of fluid dynamics. The model preserves mass and momentum, quite obviously, but its lattice and collision step are not sufficient to approximate the macroscopic solutions of the Navier-Stokes Equations. It is also interesting to note that in 1983 Wolfram[5] adapted this work on Cellular Automata to self organizing systems and categorized many of the dynamics seen on two dimensions.

The development of the lattice gas automata FHP model developed by Frisch, Hasslacher, and Pomeau [6] describes the evolution of a fluid on a hexagonal lattice. A single particle may exist on a node in any given direction, similar to the HPP model, thus every node can be populated by at most six particles. Each particle has a momentum which is transferred to the nearest neighboring node in the following time step. The evolution of the FHP model is made up of 2 phases; the collision and the streaming. The streaming step is that which was mentioned earlier when all particles and their momentums are transferred to the nearest neighboring node. The collision step is that when particles interact and their resulting momentums change directions. A simple explanation of the process is found in Figure 2. In Figure 2, we do not list those configurations which can be obtained by rotational transformation, and which are invariant under the collision process. The particle number, the momentum, and the energy are conserved in the collision process locally and exactly. And so, it is quite obvious how the evolution of the FHP model progresses. Compared to the HPP model, the FHP model leads to the Navier-Stokes Equation in the macroscopic limit. This means that as we average the momentum over the neighboring nodes the macroscopic quantities (i.e. pressure, velocity) approach those given by the Navier-Stokes Equation.

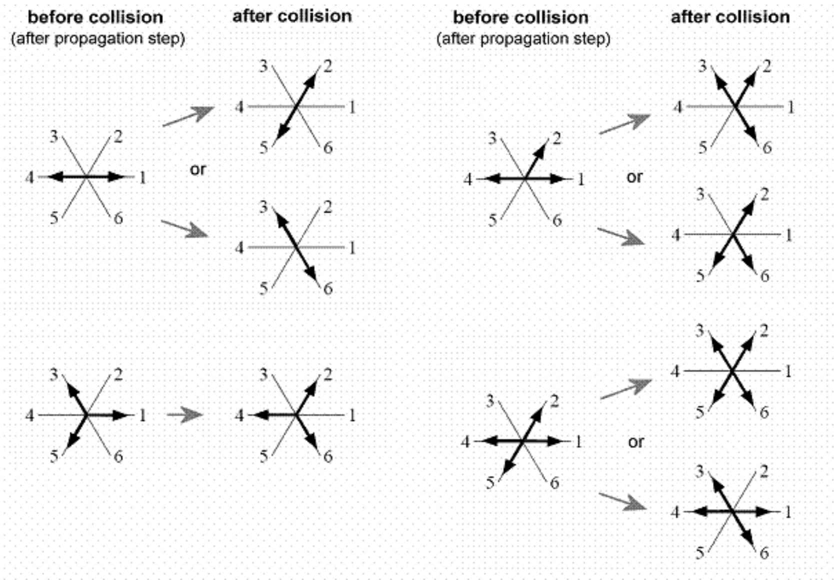

FIGURE 2: LGA Collision Step schematic. [3]

2.2 Transition to Lattice Boltzmann Method

From the Lattice Gas Automata (LGA) model it is not so difficult to conceptually shift over the the Lattice Boltzmann Method (LBM). And although the FHP model does approximate the solution of the Navier-Stokes equations to convert from the microscopic world to macroscopic quantities, used in analysis, an averaging process is necessary over local nodes. And this averaging, over essentially all nodes, is the main drawback of the FHP model as it creates statistical noise that is inherently a part of the averaging process and so cannot be eliminated. The LGA model described above is a microscopic model, in that individual particles interact and once all of these movements are put together the entirety of the flow movement can be seen. Instead of having single particles with varying velocities we take a distribution of particles, f_i, in any given direction and fix the velocity based on the lattice constants. This is why the LBM is considered a Mesoscopic Scale model, it does not model fluid dynamics with respect to macroscopic quantities such as velocity and pressure, nor does it look at the individual particles which make up the fluid (microscopic). This provides an interesting avenue conceptually as well as computationally.

Although the streaming step is identical to that of the LGA model the collision step is more involved and requires a careful derivation. In Figure 3 we see a more detailed decomposition of the LBM and the corresponding particle distribution functions f_i. One should notice that a cartesian grid is generally chosen for LBM simulations due to the relatively simple lattice constants and collision operators seen later on. This name arises from the comparison to traditional CFD methods such as Finite Difference/Element/Volume Methods and Statistical/Classical Mechanics of Particle motion, which are considered Macroscopic and Microscopic respectively.

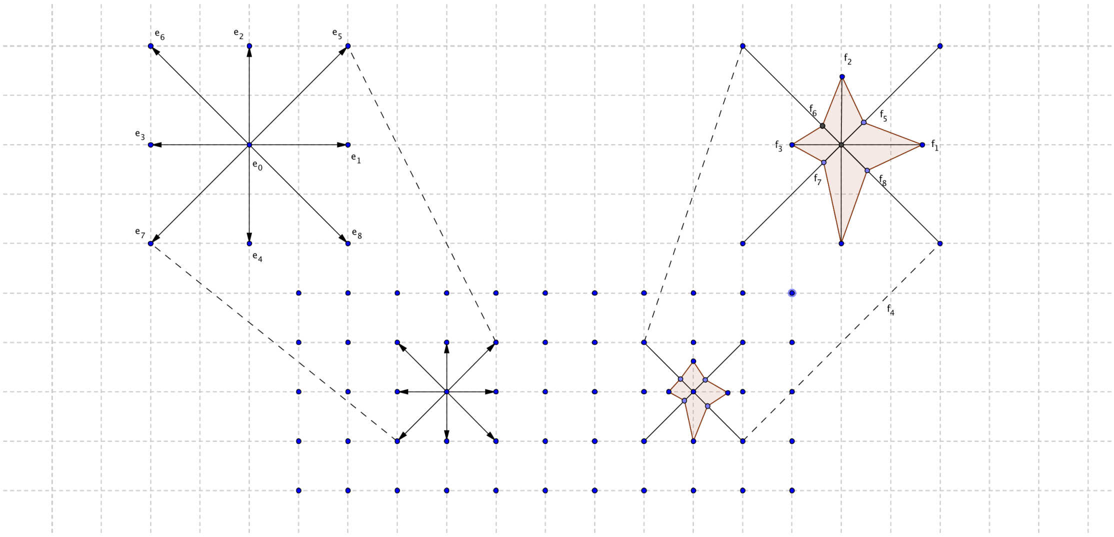

FIGURE 3: Particle distributions of the Lattice Boltzmann Method

Conceptually, to pass from these Mesoscopic quantities, f_i, to pressure and velocity at any given node one simply takes the sum of all f_i for the density, which is in a direct relationship to the pressure. One should also notice that for a density of one the sum of the f_i in Figure 3 is identically one. And to find the velocity we take the sum of the $(f_i e_i)$, where e_i are simply the unit vectors in the direction of each distribution function.

3 Derivation of the Lattice Boltzmann Method

3.1 The Boltzmann Transport Equation

In statistical mechanics and kinetic theory the flow of a fluid without external forcing is governed by the continuous Boltzmann Equation, which generally takes the following form:

$$\frac{\partial f\left(x, \vec{u}, t\right)}{\partial t} + \vec{u} \cdot \nabla f\left(x, \vec{u}, t\right) = \Omega \tag{1}$$

where $f\left(x, \vec{u}, t\right)$ is the particle distribution function, $\vec{u}$ is the particle velocity, and Ω is the collision operator. We also know that the collision of particles tends to relax the particle distribution function. This *relaxation* refers to the entropic nature of fluids to approach a state of equilibrium or balance. Thus we have that

$$\Omega = \frac{-1}{\tau}\left[f\left(x, \vec{u}, t\right) - f^{eq}\left(x, \vec{u}, t\right)\right]$$

where τ is the relaxation time and f^{eq} is the equilibrium distribution function. The equilibrium distribution is derived from the solution of the Maxwell Equations and the conservation of energy and momentum laws. This derivation is heavily rooted in Statistical Mechanics and will not be covered in this work and derivation can be found in the work of Shan et al. [7] or the original paper of Bhatnagar et al. [8]. A more interesting question which can be posed regards the equilibrium distribution function that arise from varying latices. After a simple substitution we see that our continuous time equation becomes

$$\frac{\partial f\left(x, \vec{u}, t\right)}{\partial t} + \vec{u} \cdot \nabla f\left(x, \vec{u}, t\right) = -\frac{1}{\tau}\left[f\left(x, \vec{u}, t\right) - f^{eq}\left(x, \vec{u}, t\right)\right]$$

3.2 Discretization of the Boltzmann Equation

To discretize the velocity space we introduce a finite number of velocity vectors e_i instead of the continuous velocity space $\vec{u}$, thus

$$\frac{\partial f_i\left(x, t\right)}{\partial t} + e_i \cdot \nabla f_i\left(x, t\right) = \frac{-\left[f_i\left(x, t\right) - f_i^{eq}\left(x, t\right)\right]}{\tau}$$

The discretization of the velocity space is done according to the D2Q8 or D3Q19 lattice structures, for two and three dimensions respectively, seen in Figure 4. The DαQβ

notation gives the dimension α and the number of velocity directions β. Interestingly enough the equilibrium distribution function for both of these structures is that which is given in Equation 2. Also notice that each of the lattice structures below include a vector e_0 which is the zero vector of each lattice.

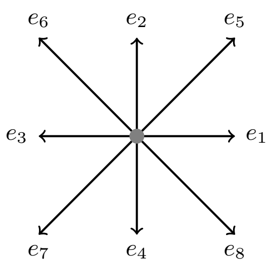

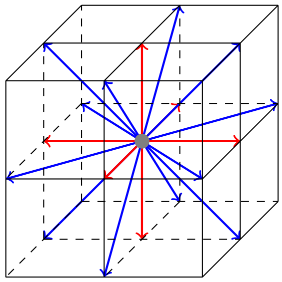

FIGURE 4: D2Q9 and D3Q19 Lattice Structures underlying LBM

For the D2Q9 and D3Q19 lattice structures and the Bhatnagar-Gross-Krook (BGK) collision model we have

$$f_i^{(eq)} = \rho t_p \left(1 + \frac{3}{c^2} e_i \vec{u} + \frac{9}{c^4} \left(e_i \vec{u}\right)^2 - \frac{3\vec{u}^2}{2c^2}\right) \tag{2}$$

where

$$t_0 = \frac{4}{9} \qquad t_p = \frac{1}{9} \quad : p = 1, 2, 3, 4 \qquad t_p = \frac{1}{36} \quad : p = 5, 6, 7, 8$$

where t_p is a weighting factor for each given lattice direction and $c = \frac{1}{\sqrt{3}}$. The velocity $\vec{u}$ is the macroscopic velocity at the given node, which is computed similarly to the macroscopic density of particles ρ:

$$\rho\left(x,t\right) = \sum_{i=0}^{8} f_i\left(x,t\right) \qquad , \qquad \vec{u}\left(x,t\right) = \frac{1}{\rho} \sum_{i=0}^{8} t_p f_i\left(x,t\right) \vec{e_i}$$

Now by using a Forward Euler Scheme we discretize time, giving:

$$\frac{\partial f_i\left(x, t+\Delta t\right)}{\Delta t} + \|e_i\|_2 \frac{f_i\left(x+\Delta x_i, t+\Delta t\right) - f_i\left(x, t+\Delta t\right)}{\|\Delta x_i\|_2} = \frac{-\left[f_i\left(x,t\right) - f_i^{eq}\left(x,t\right)\right]}{\tau}$$

where $\Delta x_i = e_i \Delta t$ and $\Delta t = 1$. These discretizations result in the explicit Lattice Boltzmann Equation, specifically when considering the BGK collision model from Equation 2 we get the Lattice Bhatnagar-Gross-Krook (LBGK) Model.

$$f_i\left(x + e_i \Delta t, t + \Delta t\right) + f_i\left(x,t\right) = \frac{-\left[f_i\left(x,t\right) - f_i^{eq}\left(x,t\right)\right]}{\tau} \tag{3}$$

3.3 The Smagorinsky Turbulent Model

The Smagorinsky Turbulent Model is an extension of the standard LBGK collision model. It enables the simulation to account for the micro-vortices which are created around simulation nodes. The LGBK model does not account for the energy lost at the molecular level due to vortices. Originally the Smagorinsky Model described in Meyers and Sagaut [9] was applied to Macroscopic methods as a *Large Eddy Simulation (LES) Model* [10], but by using *Renormalization Group (RNG) Analysis* as outlined in Liu et al. [10] we are able to incorporate the energy loss directly into the relaxation parameter τ and the non-equilibrium distribution function ($f_i^{neq} = f_i$). Considered the most widely-used LES model, the Smagorinsky model, computes a turbulent eddy viscosity v_t, estimated by

$$v_t = (C_s \Delta)^2 \left|\bar{S}\right| \tag{4}$$

where Δ is the filter size, which is equivalent to the grid spacing, and $\bar{S}$ is the resolved local strain rate. The Smagorinsky constant C_s is an adjustable parameter, generally chosen to be around 0.15 [10]. Turbulence simulation with LBM relies on the RNG analysis mentioned above, this refers to the separation of the simulation scales into two separate quantities, $f_i = \bar{f}_i + \delta f_i$, one refers to the large mean distribution functions and δf_i accounts for the sub-grid scale turbulent fluctuations [10]. Through substitution into Equation 3 we see that the δf_i is absorbed into the relaxation parameters. For the LBGK model the renormalization of the collision operator is as follows:

$$\Omega = -\frac{1}{\tau}\left(\bar{f}_i^{neq} + \delta f_i\right) = -\frac{1}{\tau + \tau_{turb}}\left(\bar{f}_i^{neq}\right)$$

Using the procedure from Filippova et al. [11] we see that the renormalization factor τ_{turb} is given by $\tau_{turb} = 3v_t$, where v_t is the turbulent eddy viscosity obtained from the macroscopic turbulence model [10]. And from here one can easily find the total relaxation parameter of the LBGK model incorporating the Smagorinsky turbulent model

$$s_{total} = (t_{total})^{-1} = (3\,(v + v_{turb}) + 0.5)^{-1} \tag{5}$$

With RNG, it is clear that to apply LBE for turbulence simulation, it is important to have appropriate prediction of the eddy viscosity and size [10]. As larger vortices and instabilities create smaller and smaller eddies around them, these *micro-vortices* transfer energy from the macroscopic lever to the microscopic level and it is *lost*, with respect to the simulation. This transfer of energy can be seen as the transformation of energy from kinetic energy to internal energy, in the form of heat. With the Smagorinsky Model we take these vortices into account and input the energy back into the simulation. As the Smagorinsky Constant is decreased the size of the micro-vortices that are taken into account is also decreased and the kinematic viscosity within these vortices is increased, as such to maintain consistency within the simulations one should also increase the resolution of the model as the Smagorinsky Constant is decreased. But in Figure 10 this was ignored to be able to better compare the resulting flow patterns. The literature generally suggests a Smagorinsky Constant ranging from 0.03 by Liu et al. [12] to 0.15 by Liu et al. [10] but in the three dimensional simulations that were run we selected a Smagorinsky Constant of 0.3.

4 Boundary Conditions

4.1 Analytical Results regarding Zero Pressure Outlet BC

The procedure detailed in Zou and He [1] gives the necessary conditions and assumptions to impose both velocity and pressure boundary conditions on a flowing boundary. By convention an outlet pressure boundary condition is imposed in most LBM simulation, and a velocity profile at the inlet to allow for time dependent simulations and easy variation of the Reynolds Number. Below we see the results of the Zou and He [1] paper when considering a pressure boundary on a vertical eastward flow boundary:

$$u_x = \frac{(f_0 + f_2 + f_4 + 2(f_1 + f_5 + f_8))}{\rho} - 1 \tag{6}$$

$$f_6 = f_8 + \frac{1}{2}(f_4 - f_2) - \frac{\rho u_x}{6} \tag{7}$$

$$f_7 = f_5 + \frac{1}{2}(f_2 - f_4) - \frac{\rho u_x}{6} \tag{8}$$

$$f_3 = f_1 + \frac{2}{3}(\rho u_x) \tag{9}$$

Notice that in this case we are specifying a density $\rho = 1$ as well as assuming that the vertical component of the velocity, u_y is identically zero. The components f_1, f_5, and f_8 are know because they follow from the previous streaming step to the current nodes on the boundary. Now with these assumptions, the boundary condition taken into account and the unknowns solved for, we reverse the boundary. Meaning that we assume the same nodes to act as a pressure boundary condition only in the opposite direction (as a western boundary). And we compute the corresponding velocity in that direction u'_x, noting that the vertical component is still assumed to be zero. This gives

$$u'_x = 1 - \left[(f_0 + f_2 + f_4) + 2\,(f_3 + f_6 + f_7)\right] \tag{10}$$

and Equations (5), (6), and (7) from above become:

$$f_6 = f_8 + \frac{1}{2}\,(f_4 - f_2) - \frac{1}{6}\,(f_0 + f_2 + f_4) - \frac{1}{3}\,(f_1 + f_5 + f_8) + \frac{1}{6} \tag{11}$$

$$f_7 = f_5 + \frac{1}{2}\,(f_2 - f_4) - \frac{1}{6}\,(f_0 + f_2 + f_4) - \frac{1}{3}\,(f_1 + f_5 + f_8) + \frac{1}{6} \tag{12}$$

$$f_3 = f_1 - \frac{2}{3}\,(f_0 + f_2 + f_4) - \frac{4}{3}\,(f_1 + f_5 + f_8) + \frac{2}{3} \tag{13}$$

We now substitute these distributions into the equation for u'_x to arrive at

$$\begin{aligned} u'_x = 1 - (f_0 + f_2 + f_4) - 2[(f_1 + f_5 + f_8) \\ - (f_0 + f_2 + f_4) - 2\,(f_1 + f_5 + f_8) + 1] \end{aligned} \tag{14}$$

which ultimately gives

$$u'_x = f_0 + f_2 + f_4 \tag{15}$$

This essentially means that for a pressure boundary condition of this type we notice a *backwards* propagation of velocity solely dependent on the distribution functions parallel to the boundary. For most simulations where the majority of flow is perpendicular to the flow boundary this is not an issue; but in the stenotic geometry where the vortices created post-stenosis have a large vertical velocity component it may explain the difficulty in the stabilization of flows.

The plots in Figure 5 were created with a very high contrast to better visualize the transition of the velocity patterns. And although subfigures (A) and (B) are only separated by one time point, they show vastly different patterns. This leads to the conclusion that in flows where the velocity in the Y-Direction varies significantly over short time periods the Pressure Boundary condition proposed by Zou and He [1] break down.

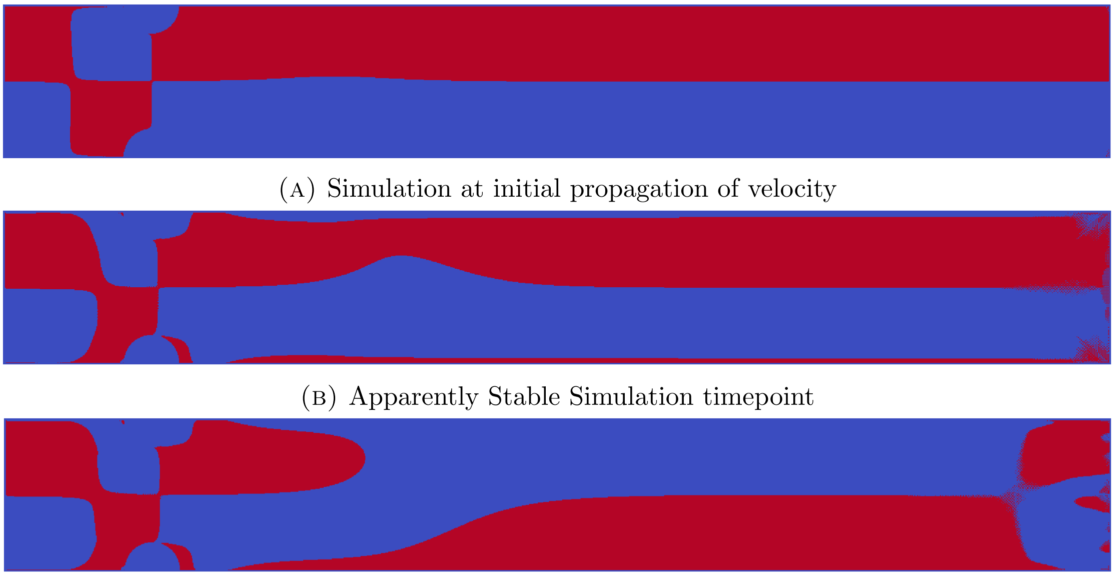

(A) Simulation at initial propagation of velocity

(B) Apparently Stable Simulation timepoint

(C) Simulation just before Blow-up

FIGURE 5: Plots of Magnitude of velocity in the Y-Direction with Zou and He [1] Pressure Boundary

4.2 Analytical Results regarding Constant Velocity Outlet BC

To provide an additional level of verification of the above hypothesis let us investigate the resulting *backwards* propagation of flow with a velocity boundary. Now instead of fixing the density, ρ at the outlet we fix the horizontal velocity, u_x (and still set $u_y = 0$). This results in

$$\rho = \frac{(f_0 + f_2 + f_4 + 2\,(f_1 + f_5 + f_8))}{1 - u_x}$$
$$f_6 = f_8 + \frac{1}{2}\,(f_4 - f_2) - \frac{\rho u_x}{6}$$
$$f_7 = f_5 + \frac{1}{2}\,(f_2 - f_4) - \frac{\rho u_x}{6}$$
$$f_3 = f_1 + \frac{2}{3}\,(\rho u_x)$$

From here onwards we follow a procedure exactly as above for the pressure boundary condition. We reverse the boundary and consider a pressure boundary on the same nodes only in the opposite direction, towards the western part of the geometry. After simplification this results in

$$u_x' = 1 - \frac{2}{1 - u_x}\,[f_0 + f_2 + f_4 + 2\,(f_1 + f_5 + f_8)] = 1 - 2\rho \tag{16}$$

this relationship between the local density and the *backwards* propagation of flow is interesting because for the initial conditions that $\rho = 1$ at all nodes it results in a negative velocity. And from this reference point a negative velocity means in the direction of the outflow, opposite to the results of the pressure boundary condition. Even further, using the relation $P = c\,(1 - \rho)$ where P is the pressure, and $c = \frac{1}{\sqrt{3}}$ for the local pressure we can deduce that the velocity boundary in two dimensions using the LBGK collision model will only produce a *backwards* propagation of flow for an outlet pressure of 0.29 (Which is equivalent to a density of 0.5), which is not physically viable with the initial conditions of constant pressure zero.

5 Implementation and OpenLB

For this work the open source library OpenLB was used for computation. OpenLB is currently maintained by the Karlsruhe Institute of Technology in Germany. Specifically the 0.9 Release of the code is being used. The main advantages of this library for my work were the inclusion of the Smagorinsky Turbulent Model, the STL reader capabilities, and the OpenMPI parallelization capabilities. The Smagorinsky Turbulent Model was primarily used in the three dimensional geometries to maintain stability and ensure an accurate simulation. The Standard Tessellation Language (STL) reader implemented within the library allows one to simply create an STL file using a Computer Aided Design (CAD) software and once the surface normals and centers are known the simulation can be computed within the given geometry. Specifically, the Arched Stenosis geometry seen in Figure 14 was created using the software Inventor Professional from the Autodesk community and a free student license. Lastly, the OpenMPI functionality allows us to take full advantage of the parallelization capabilities of the LBM [13]. These particular aspects make the set-up and computation of the simulations significantly faster and more accurate. The overall outline of the functions used within the code, is structured as seen below:

```
void prepareGeometry( converter,  indicator, stlReader, superGeometry)
                                               { ... }

void prepareLattice(sLattice, converter, bulkDynamics, bc, offBc,
                                               stlReader, superGeometry)  { ... }

void setBoundaryValues(sLattice, converter, iT, maxPhysT,
                                               OffLatticeBoundaryCondition)
                                               { ... }

void getResults( Lattice, converter, iT,  timer)   { ... }
```

The names of the functions seen in the code are quite self explanatory; prepareGeometry, prepareLattice, setBoundaryValues, and getResults. Then, these functions are simply called directly within the main part of the code where the appropriate variables are passed. For now, the flow rates extracted from Figure 12 are hardcoded into the simulation as a text file, this means that the flow rates exported from MEVIS Flow are imported into an array and the code interpolates these values using a Catmull-Rom Spline, explicitly derived by Catmull and Rom [14], which are then passed to the setBoundaryValues function.

The function getResults both prints status updates to the console as well as vti files corresponding to each iteration point which can be viewed with ParaView. The status updates that I choose to output are the average velocity and pressure throughout the geometry and the lattice velocity at three distinct points; near the inlet, near the outlet, and at the stenosis. These real time outputs allow me to see whether the simulation is progressing as planned or if adjustments need to be made.

6 Two Dimensional Results

In Figure 6 we see the stabilization results, or rather lack thereof, that were found using a hardcoded Lattice Boltzmann Method simulation done in C++. The Reynolds numbers that are seen are computed with respect to the peak velocity within the stenosis. In these simulations a Poisseuille velocity boundary condition was imposed at the inlet and a Pressure boundary condition was imposed at the outlet, as described by Zou and He [1] along with standard bounce back along the stenotic walls. Each subfigure provides a plot of the velocity magnitude on top and the pressure on the bottom.

The consistent pressure drop that is seen in all subfigures of Figure 6 is consistent with experimental results and other simulations of stenotic geometries, but all have the same issue of premature blowup origination at the outflow pressure boundary. As such, simulations were performed with outlet velocity boundary conditions. The results are seen below in Figure 7, please note that the difference in color schemes is due to the use of the OpenLB Library and consequently the analysis tool ParaView.

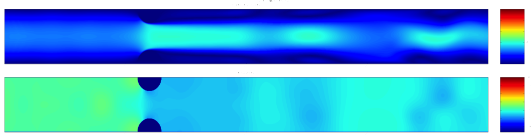

(A) Simulation at Re=1114

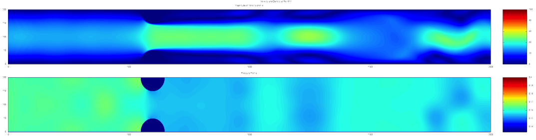

(C) Simulation at Re=1286

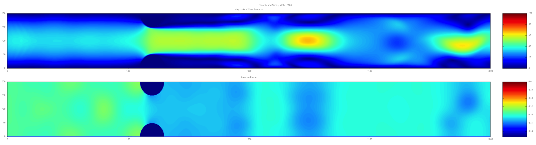

(B) Simulation at Re=1486

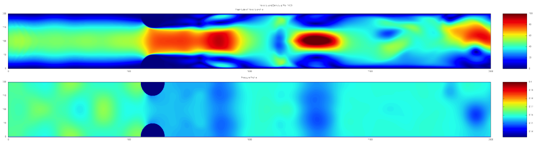

(D) Simulation at Re=1857

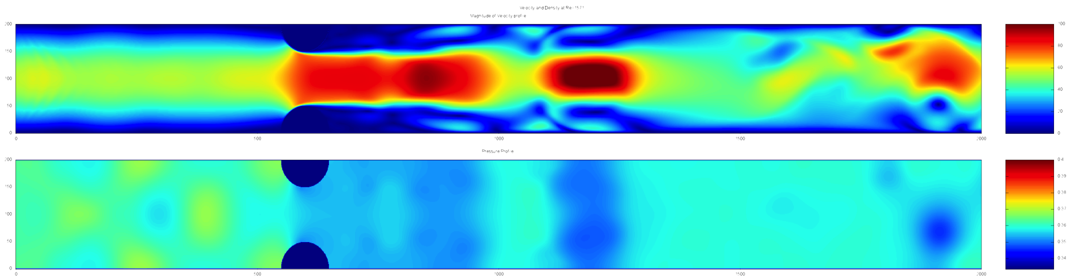

(E) Simulation at Re=2429

FIGURE 6: Simulations carried out without OpenLB in Fall 2014

6.1 Experimental Results concerning Boundary Conditions

It is quite obvious from the plots in Figure 7 that the outlet velocity boundary conditions are significantly more stable. And these results are only with a fixed outlet velocity not dependent on the geometry or dynamics. The next step was to create a model that varies even in two dimensions and adapts to the given geometry and Reynolds Number. The most stable simulation turned out to be that where we extract the velocity at the stenotic boundary for the length of the start-up period, then fix it at the last lattice velocity. The results are exactly what we were searching for with the previous simulations, where the pressure boundary conditions did not allow us to verify that the given Reynolds numbers created periodic flow patterns.

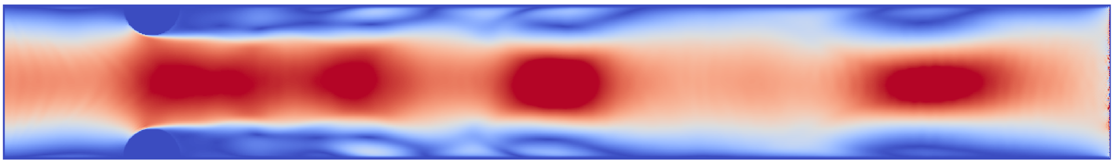

(A) Simulation with the original 0 pressure boundary condition

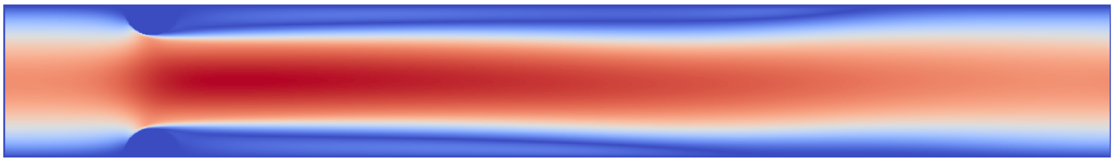

(B) Simulation where outlet velocity is equal to inlet velocity

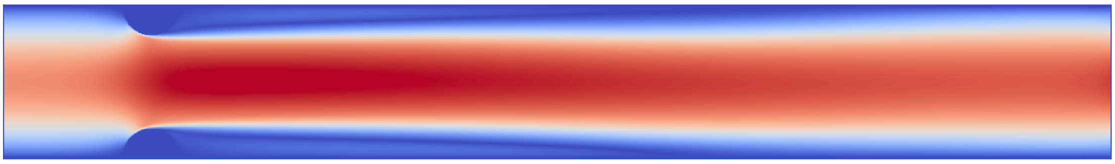

(C) Simulation with (outlet velocity) = 1.2(inlet velocity)

FIGURE 7: Plots of Velocity Magnitude at reported Reynolds Number of 875

The periodic flow patterns mentioned above are seen in Figure 8. The subfigures show multiple iteration of the same simulations to show how the simulation is periodic within the time domain, as theorized for the transition period of Reynolds Numbers. Specifically in Figure 8 the velocity outlet is determined by the lattice velocity from the previous time-step at the stenosis.

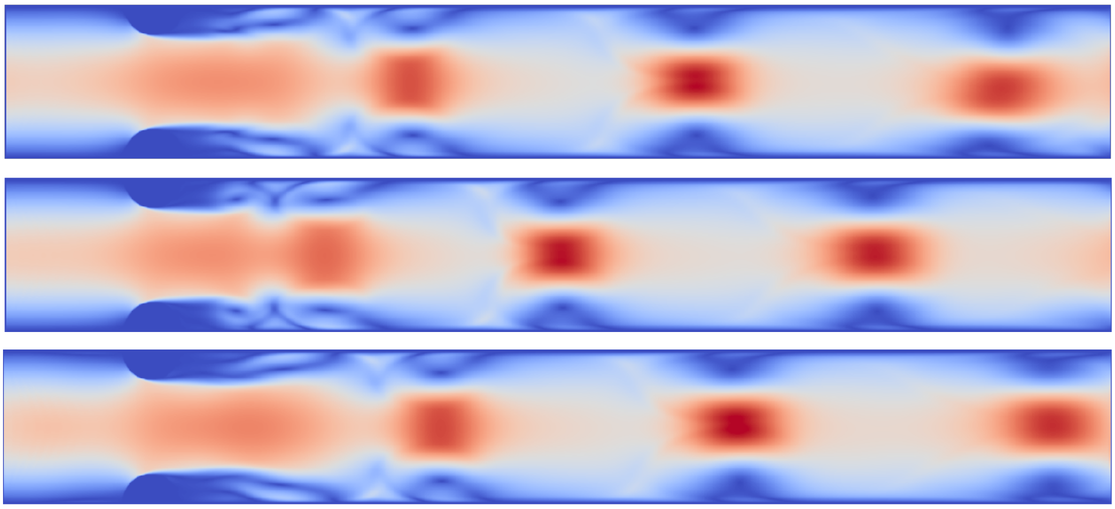

FIGURE 8: Multiple Iterations of Velocity Magnitude at Reynolds Number of 1000 exhibiting Periodic Flow

The *periodic* flow pattern seen above is characterized by the fact that the bottom plot is almost identical to the top plot while being separated by 40 iterations. This is an interesting development for the analysis of two dimensional stenotic flows because it clearly shows the existence of a non-turbulent yet non-laminar stabilization.

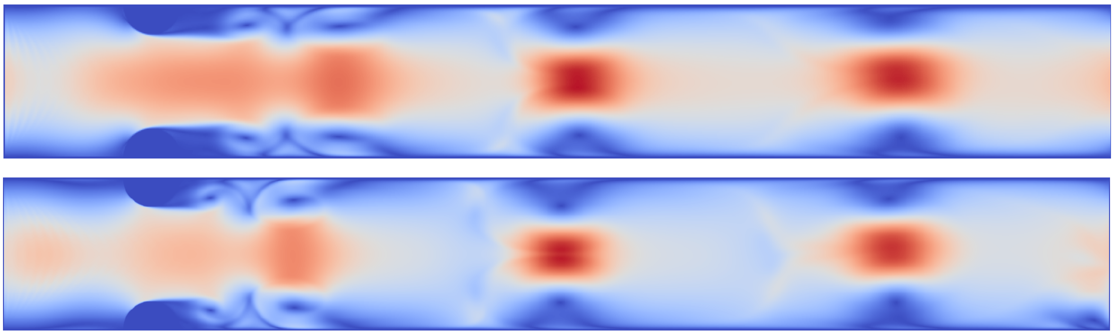

Figure 9: Periodic Velocity Pattern at Reynolds Number 1000(Above) and 1500(Below) with Velocity Outlet Boundary

As you can see in Figure 9, even at larger Reynolds numbers the boundary conditions hold up and give clear results as to the dynamics that occur for this given geometry. Namely, as the Reynolds Number increases, the periodic flow phenomena become more distinct and at a higher frequency.

6.2 The Smagorinsky Turbulent Model

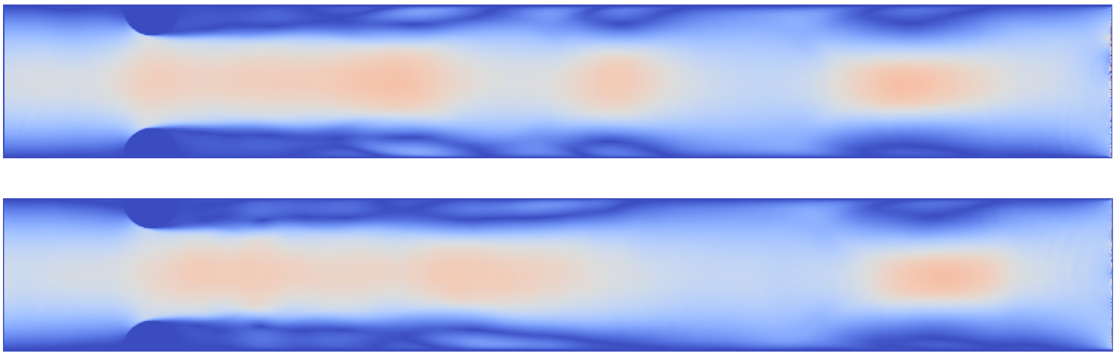

Figure 10: Simulation of Reynolds Number 1000 geometry with Pressure Boundary and Smagorinsky constants 0.2(Top) and 0.1(Bottom)

In Figure 10 the two simulations are identical except for the Smagorinsky Constant which is varied from 0.2 to 0.1. The flow patterns in Figure 10 are consistent with the theory detailed in Section 3.3. Namely, for the lower Smagosinsky Constant the flow is more stable and the periodic regions are spread farther apart, also it appears that the flow in the lower simulation may even reattach to the walls, which is very rare in the LBGK model at such a Reynolds Number.

7 Experimental Data

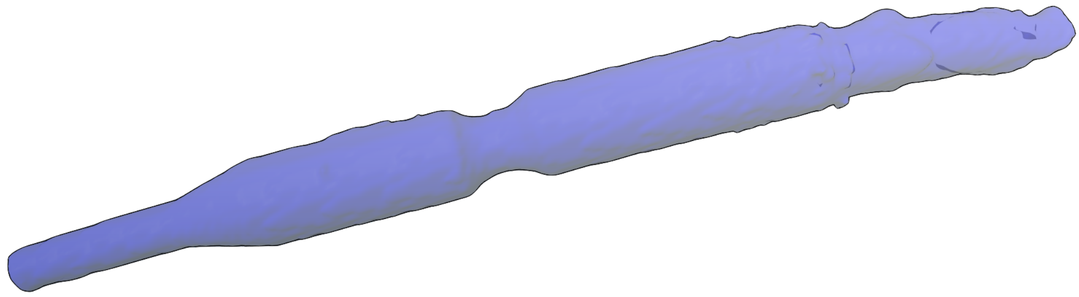

FIGURE 11: Freiburg Ghost Stenosis Segmentation

The mask seen in Figure 11 is what was used to generate the inlet and outlet velocity profiles used in the three dimensional simulations. Specifically the Velocity profile seen in Figure 12 is taken from the right hand side of the mask seen in Figure 11. From this physical model an STL file was created with similar dimensions. The mask seen in Figure 11 is the result of an experiment to extract flow rates using 4D Flow MRI, as such a physical model was created and this is the digital representation.

7.1 Inlet Velocity Profile

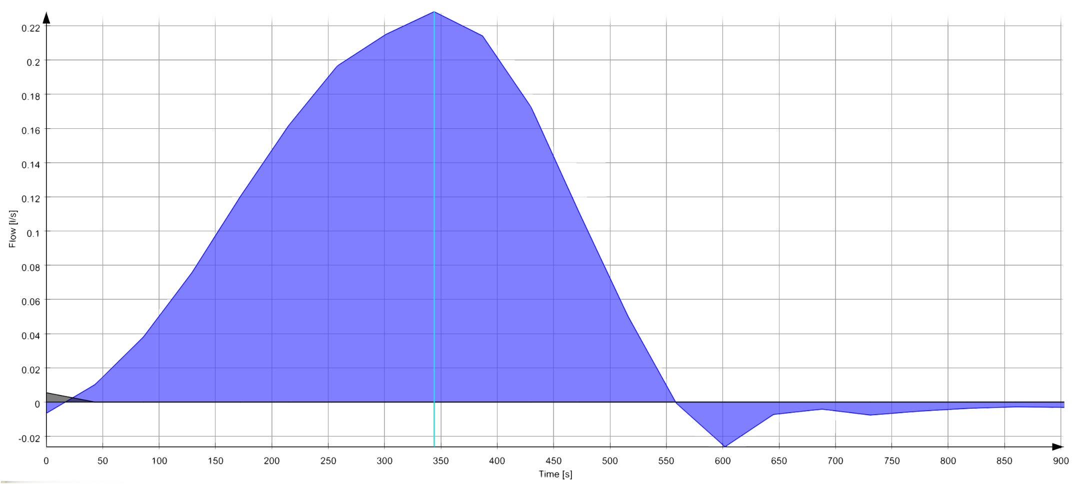

FIGURE 12: Velocity profile at the Inlet Boundary

The curve seen in Figure 12 is a time dependent plot of the velocity taken just to the right of the stenosis in Figure 11 and the vertical blue line marks the max systole of a cardiac cycle. The point where the flow rate is maximal and the heart is completely contracted. Using an interpolation of this curve we impose a Poiseuille Velocity profile at the Inlet of the three dimensional geometries. One should also note that a similar procedure to that which is used to extract inlet velocity profiles was followed to extract the outlet velocity profiles used later in the Velocity Boundary simulations.

7.2 Relative Pressure at Peak Systole

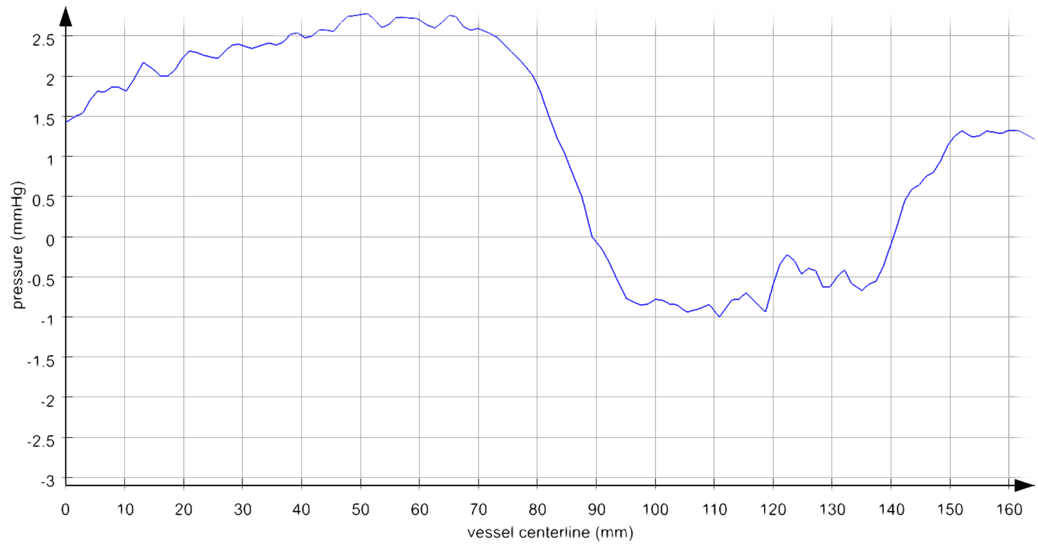

FIGURE 13: Plot of Relative Pressure along the centerline, with zero reference point taken at Stenosis

The plot in Figure 13 is the relative pressure through the centerline of the Freiburg Ghost Stenosis with the zero taken at the stenotic point. The point of interest is the drop in pressure located around the 70mm mark. The total pressure drop appears to be slightly greater than 3.5mmHg. The fluctuations seen in the plot arise from the non-smooth boundary that was extracted from the MRI data.

8 Three Dimensional Results

8.1 Geometry Simplifications

As the aorta is a complicated geometry with many specifications beyond the research scopes of this thesis we simplify it quite significantly. Namely, in Figure 14 we take the aortic segmentation being used by Dr. Hanieh Mirzaee at Fraunhofer MEVIS and simplify it into two separate geometries upon which we will carry out our analysis. One should also note that from here onwards all relative pressure plots were computed using the Poisson Equation given the velocity taken from simulation at any given point.

This means that the relative pressure seen is not computed directly from the simulation results but there is an additional processing step before we could visualize such results.

FIGURE 14: Simplification of Aortic Stenosis

8.2 Simple Stenosis with Pressure Outlet

The geometry seen on the Right in Figure 14 is what was used to generate the simulation of the simplified three dimensional stenosis. One fact to keep in mind is that all units are in meters and the mesh files loaded into OpenLB must be capped, meaning that the inlet and outlet must also have surfaces. The extended length following the stenosis is done to increase stability and decrease outlet effects on the dynamics surrounding stenosis.

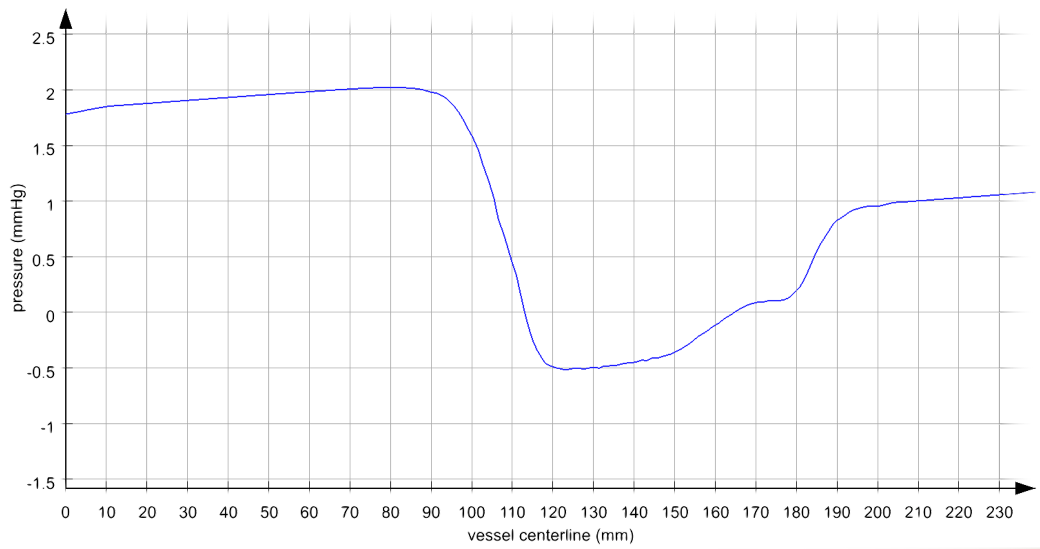

FIGURE 15: Plot of Relative Pressure along the centerline, with zero reference point taken at Stenosis. For Simple Stenosis with Pressure Boundary

The total pressure drop appears to be approximately 2.5mmHg in Figure 15. Compared to the relative pressure drop extracted from the MRI data this plot is significantly smoother while still maintaining the same structure. The initial pressure drop at stenosis is smaller than that of the MRI data. Then it begins to level out to an intermediate pressure before it stabilizes to the outlet pressure. It is worthwhile to note that this is not clearly visible in the MRI data but using these results we can interpret the MRI data better as well.

8.3 Simple Stenosis with Velocity Outlet

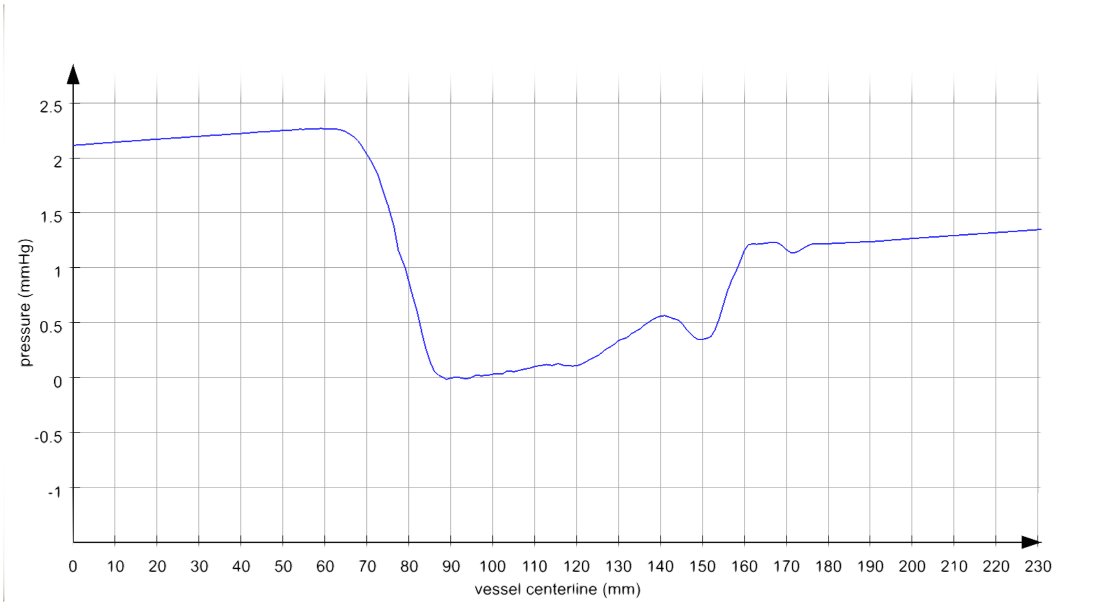

FIGURE 16: Plot of Relative Pressure along the centerline, with zero reference point taken at Stenosis. For Simple Stenosis with Velocity Boundary

The total pressure drop appears to be slightly less than 2.5mmHg in Figure 16. Here we notice an even smaller relative pressure drop, but one should also notice that it is steeper than the others for similar geometries. While these facts would point to a more stable simulation with a velocity outlet profile, the relative pressure in this simulation actually has more instabilities following the stenosis compared to the Pressure outlet profile.

From these two graphs, Figures 15 and 16, we notice that the simulations using the geometry on the right in Figure 14 produce relative pressure differences significantly less that the original MRI data. This can be attributed to the increased smoothness of the geometry as well as the extended outlet. In Figures 17 and 18 we see frames of streamlines colored by the magnitude of the velocity taken at peak systole, as seen in Figure 12.

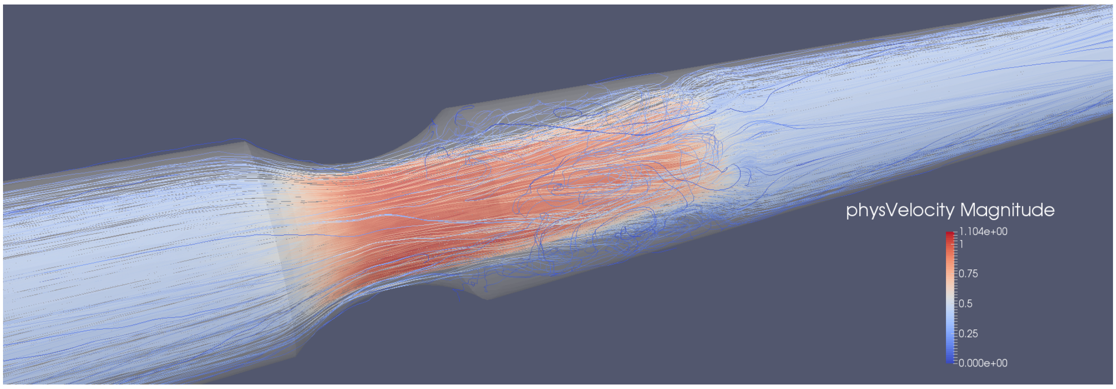

FIGURE 17: Streamlines of Simplified Stenosis at Peak Systole with Pressure Boundary

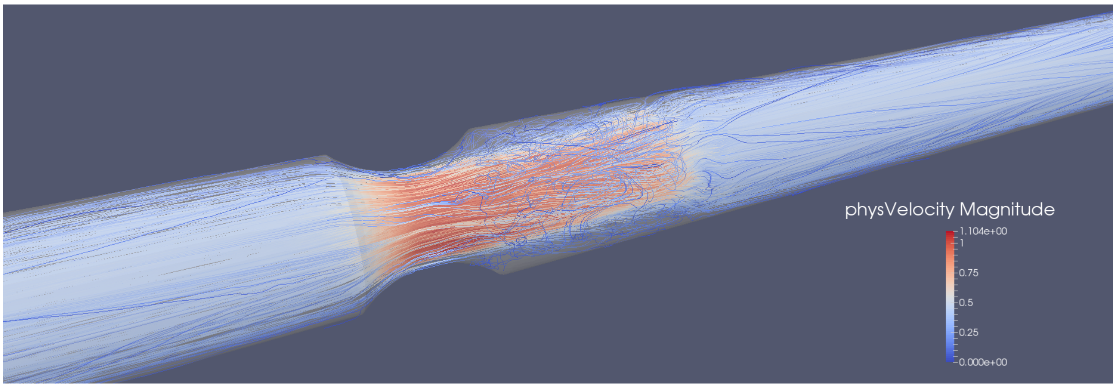

FIGURE 18: Streamlines of Simplified Stenosis at Peak Systole with Velocity Boundary

8.4 Arched Stenosis Simulations

The geometry seen in the middle of Figure 14 is what was used to generate the simulation of the simplified three dimensional arched stenosis. The extended length following the stenosis is done to increase stability and decrease outlet effects on the dynamics surrounding stenosis.

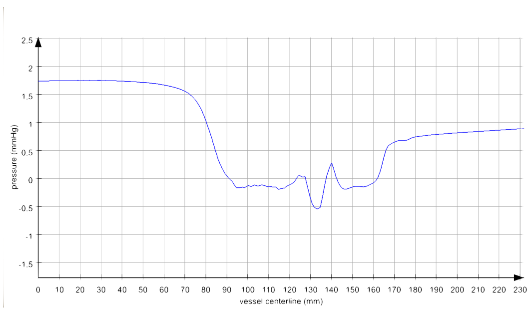

(A) Plot for Arched Stenosis with Pressure Boundary

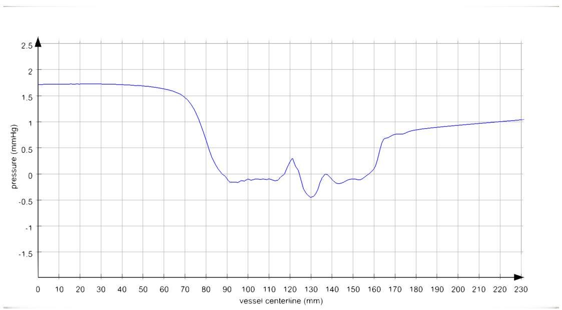

(B) Plot for Arched Stenosis with Velocity Boundary

FIGURE 19: Plot of relative pressure along the centerline, with zero reference point taken at Stenosis for the Arched Stenosis Geometry.

From the plots in Figure 19 we notice that the simulations using the arched stenosis geometry from the middle of Figure 14 produce relative pressure differences significantly less that the original MRI data or the results from the simple stenotic geometry. This can be attributed to the dissipation of the velocity following the stenosis due to the arch preceding the stenosis. This means that because the geometry is curved before the stenosis the increased velocity at the stenosis cannot propagate forward as it did in the previous geometries. This is also seen in the fluctuations after the pressure drop, which can be seen more clearly in the following figures. In Figures 20 and 21 we see frames of streamlines colored by the magnitude of the velocity taken at peak systole, as seen in Figure 12.

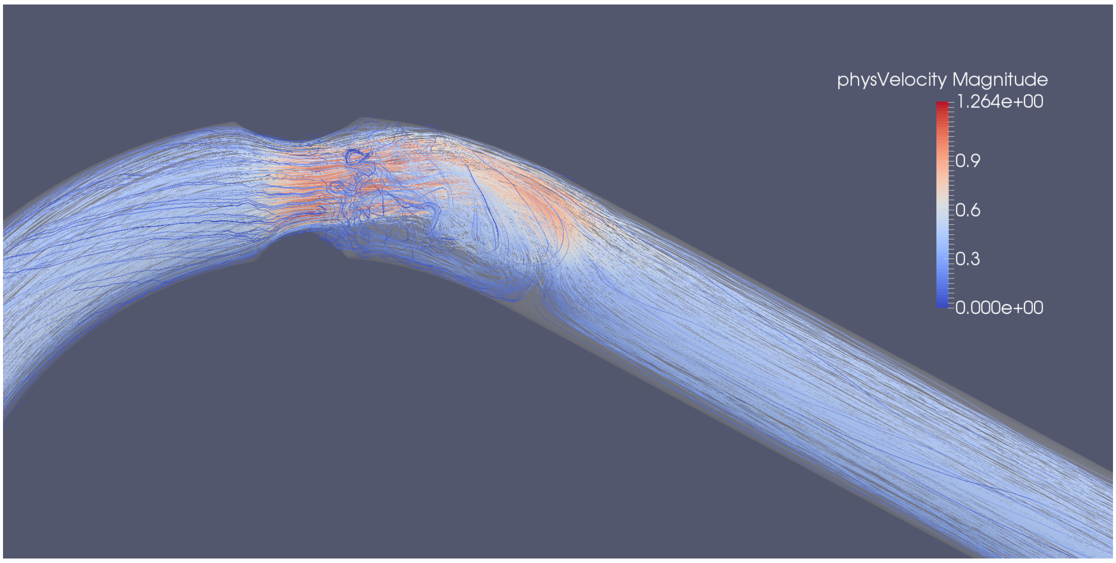

Figure 20: Streamlines of Arched Stenosis at Peak Systole with Pressure Boundary

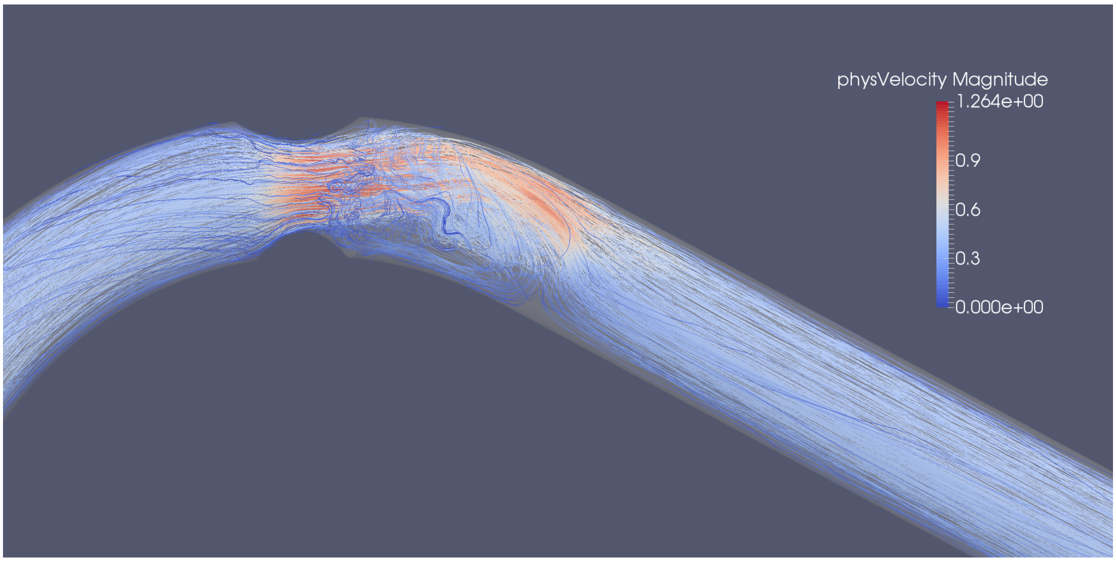

Figure 21: Streamlines of Arched Stenosis at Peak Systole with Velocity Boundary

9 Conclusions

From the multitude of simulations that were run we were able to extract multiple interesting results. In two dimensions we investigated the effects of the outlet boundary condition both from a theoretical standpoint as well as an experimental one, and we found that in the geometry of a stenotic channel the velocity outlet boundary condition greatly outperforms the pressure outlet boundary condition. Also the analysis of the *backwards* propagation of velocity waves leads us to new insights about the origins of the instability seen in the simulations using the zero pressure outlet boundary. Using these results, we constructed a model which varies the outlet velocity based on the lattice velocity at the stenosis. This model was then used to find range of Reynolds numbers for which flow is neither laminar nor turbulent. Namely, this transition period where periodic flow patterns are found was analyzed and found to range from a Reynolds number of 1000 to 2000 after which the flow begins to exhibit turbulent characteristics. Also in two dimensions, a short analysis of the effect of the Smagorinsky Turbulent model was done. With the inclusion of the Smagorinsky model, the simulation appeared to stabilize without the occurrence of periodic flow patterns leading us to believe that certain properties of flow were lost with the inclusion of the Smagorinsky model.

In the three dimensional scenario we analyzed two specific geometries; the simple stenosis and the arched stenosis. Here we also had the opportunity to compare our results with the 4D Flow MRI data from Freiburg. After comparing the relative pressure drops found in the MRI data and our simulations we noticed significantly lower relative pressure drops across the stenosis. This fact can be attributed first to the smoothness of the geometries and secondly to the geometries themselves. Meaning that even in the simple stenosis case our outlet was located much further from the stenosis than in the experimental data, and in the arched stenosis case the obvious differences are the areas preceding the stenosis where an arch exists. But these results are positive in the fact that a pressure drop was recorded and following the stenosis in both geometries physically meaningful results were found from analyzing the streamline patterns.

10 Future Work

Further work on the two dimensional case involves the variation of the stenotic degree. This would additionally verify the results found regarding the boundary conditions as well as the transition period of Reynolds numbers. Also a possible modification of the code to run time dependent simulations with non-constant variation in the initial velocity at the inlet may provide interesting results and parallels to the three dimensional case.

In the case of the three dimensional geometries additional analysis of the relative pressure plots may yield insights into the medical capabilities of our model. Namely, using additional software to simulate the addition of a stent within the artery we could analyze the flow before and after treatment and give more definitive results regarding the effectiveness. Also because the relative pressure is computed from the velocity extracted from simulation, there may exist numerical errors that we cannot see in these plots. Therefore more work needs to be done to accurately analyze the pressure within the simulation without the need of additional software. And lastly similarly to the two dimensional case varying degrees of stenosis may yield interesting results. But to make any of these findings significant a Resolution Analysis also needs to be completed to verify the resolution needed to produce stable results without significant numerical error.

References

[1] Qisu Zou and Xiaoyi He. On pressure and velocity boundary conditions for the lattice Boltzmann BGK model. *Phys. Fluids*, 9:1591–1598, 1997. doi: 10.1063/1.869307.

[2] Zoran Stankovic, Bradley D. Allen, Julio Garcia, Kelly B. Jarvis, and Michael Markl. 4d flow imaging with mri. *Cardiovascular Diagnosis and Therapy*, 4(2), 2014. ISSN 2223-3660. URL `http://www.thecdt.org/article/view/3630`.

[3] D Raabe. Overview of the lattice boltzmann method for nano- and microscale fluid dynamics in materials science and engineering. *Modelling and Simulation in Materials Science and Engineering*, 12(6):R13, 2004. URL `http://stacks.iop.org/0965-0393/12/i=6/a=R01`.

[4] J. Hardy, Y. Pomeau, and O. de Pazzis. Time evolution of a two-dimensional classical lattice system. *Phys. Rev. Lett.*, 31:276–279, Jul 1973. doi: 10.1103/PhysRevLett.31.276. URL `http://link.aps.org/doi/10.1103/PhysRevLett.31.276`.

[5] Stephen Wolfram. Statistical mechanics of cellular automata. *Rev. Mod. Phys.*, 55:601–644, Jul 1983. doi: 10.1103/RevModPhys.55.601. URL `http://link.aps.org/doi/10.1103/RevModPhys.55.601`.

[6] U. Frisch, B. Hasslacher, and Y. Pomeau. Lattice-gas automata for the navier-stokes equation. *Phys. Rev. Lett.*, 56:1505–1508, Apr 1986. doi: 10.1103/PhysRevLett.56.1505. URL `http://link.aps.org/doi/10.1103/PhysRevLett.56.1505`.

[7] Xiaowen Shan, Xue-Feng Yuan, and Hudong Chen. Kinetic theory representation of hydrodynamics: a way beyond the Navier–Stokes equation. *J. Fluid Mech.*, 550:413–441, 2006.

[8] P. L. Bhatnagar, E. P. Gross, and M. Krook. A model for collision processes in gases. i. small amplitude processes in charged and neutral one-component systems. *Phys. Rev.*, 94:511–525, May 1954.

[9] Johan Meyers and Pierre Sagaut. On the model coefficients for the standard and the variational multi-scale smagorinsky model. *Journal of Fluid Mechanics*, 569:287–319, 12 2006. ISSN 1469-7645.

[10] Xiaopei Liu, Wai-Man Pang, Jing Qin, and Chi-Wing Fu. Turbulence simulation by adaptive multi-relaxation lattice boltzmann modeling. *IEEE Trans. Vis. Comput. Graph.*, 20(2):289–302, 2014.

[11] Olga Filippova, Sauro Succi, Francesco Mazzocco, Cinzio Arrighetti, Gino Bella, and Dieter Hanel. Multiscale Lattice Boltzmann Schemes with Turbulence Modeling. *Journal of Computational Physics*, 170(2):812–829, July 2001.

[12] Xiaopei Liu, Wai-Man Pang, Jing Qin, and Chi-Wing Fu. Turbulence simulation by adaptive multi-relaxation lattice boltzmann modeling. *IEEE Transactions on Visualization and Computer Graphics*, 20(2):289–302, February 2014. ISSN 1077-2626. doi: 10.1109/TVCG.2012.303. URL `http://dx.doi.org/10.1109/TVCG.2012.303`.

[13] M.J. Krause, V. Heuveline, and J. Latt. Towards a hybrid parallelization of lattice boltzmann methods. *Computers and Mathematics with Applications*, 2009.

[14] E. Catmull and R. Rom. A class of local interpolating splines. *Computer aided geometric design. Academic Press.*, pages 317–326, 1974.

[15] Yuanxun Bill Bao and Justin Meskas. Lattice Boltzmann Method for Fluid Simulations. *Courant Institute of Mathematical Sciences*, 2011.

[16] Sandor Ianos Bernad, Romeo Susan-Resiga, and Dan Bernad, Elenaand Gaita. 3d simulation of the blood flow in arterial stenosis. *Tohoku Mathematical*, 55:No. 2, 2005. doi: 10.2748.

[17] S. Ul Islam, C. Y. Zhou, A. Shah, and P. Xie. Numerical simulation of flow past rectangular cylinders with different aspect ratios using the incompressible lattice boltzmann method. *Journal of Mechanical Science and Technology*, 26:1027–1041, 2012. doi: 10.1007.

[18] M. Van Dyke. An album of fluid motion. *The Parabolid Press*, page 29, 1982.

[19] Max-Planck-Institut fur Eisenforschung GmbH. Lattice Boltzmann Fluid Dynamics, 2008. URL `http://www.mpie.de/index.php?id=1208&type=1`.

[20] Jeffrey Yepez, Guy P. Seeley, and Norman H. Margolus. Lattice-gas automata fluids on parallel supercomputers, 1993.

[21] Dragos B. Chirila. Introduction to lattice boltzmann methods, 2010.

[22] V. Heuveline and J. Latt. The openlb project: An open source and object oriented implementation of lattice boltzmann methods. *International Journal of Modern Physics C*, 18(4):627–634, 2007.